

Valence state of titanium in the Wark–Lovering rim of a Leoville CAI as a record of progressive oxidation in the early Solar Nebula

Kathryn A. Dyl^{a,*}, Justin I. Simon^{b,c}, Edward D. Young^{a,d}

^a Department of Earth and Space Sciences, UCLA, Los Angeles, CA 90095, United States

^b Center for Isotope Geochemistry, UC Berkeley, Berkeley, CA 94720, United States

^c Berkeley Geochronology Center, Berkeley, CA 94709, United States

^d Institute of Geophysics and Planetary Physics, UCLA, Los Angeles, CA 90095, United States

Received 15 October 2009; accepted in revised form 23 September 2010; available online 31 October 2010

Abstract

Simon et al. (2005) reported low Ti^{3+}/Ti^{4+} values in Ti-rich pyroxenes in the Wark–Lovering rim (WL) of a Leoville CAI (144A) as compared to the interior of the inclusion. These electron microprobe analyses were interpreted as evidence that the growth of the WL rim is the manifestation of an evolution to a more oxidizing environment. Further work by Simon et al. (2007) used XANES analyses to argue for higher Ti^{3+} abundances and interpreted the data of Simon et al. (2005) as the result of X-ray contamination by neighboring phases, specifically spinel. Late-stage alteration was also included as a possible explanation.

To investigate further the oxidation state of Ti in WL rims, we re-analyzed Leoville 144A to obtain a more complete data set of Ti^{3+}/Ti^{4+} values in the Wark–Lovering rims. We conducted experiments on spinel-mixing to determine whether this was a plausible explanation for the observed paucity of Ti^{3+} in WL rims. While we found a wider range of Ti^{3+}/Ti^{4+} in these WL rim data than in our original study, our new data show that the original conclusion that rims are lower in Ti^{3+}/Ti^{4+} than interiors remains valid. We conclusively rule out spinel-mixing as an explanation for our data, and we see no clear inconsistency between our electron microprobe data and the XANES data. The WL rim of CAI Ef3 was also analyzed by EMPA and compared to the results of Leoville 144A.

To predict compositional consequences of this hypothesis, we constructed a reaction space between Ti-rich pyroxene in the WL rim, perovskite, $Mg_{(g)}$, $Ca_{(g)}$, $O_{2(g)}$, and $SiO_{(g)}$. We find the oxidation of Ti^{3+} , coupled with Ti loss via perovskite formation, explains many features of WL rim EMPA analyses. We maintain that the WL rim pyroxenes are compositionally distinct from those in the interior, and are evidence of a more oxidizing environment during WL rim formation.

© 2010 Elsevier Ltd. All rights reserved.

1. INTRODUCTION

Calcium–aluminum-rich inclusions (CAIs) provide an essential record of processes that occurred in the early solar nebula. Their isotopic anomalies, primordial ages (~4.568 Ga), and elemental compositions imply that they formed under nebular conditions prior to rocky planet for-

mation (Clayton et al., 1973; Grossman, 1975; Amelin et al., 2002). A key characteristic of CAIs is that as much as 67% of total Ti in Ti-bearing pyroxene is present as Ti^{3+} (Dowty and Clark, 1973; Beckett and Grossman, 1986) whereas the more oxidized 4^+ valence state is common in terrestrial rocks. The abundance of Ti^{3+} in CAI pyroxene indicates formation in an extremely reducing environment, corresponding to oxygen fugacities (fO_2) at or below those defined by an H_2 -rich gas of solar composition (Stolper et al., 1982; Krot et al., 2000).

Many CAIs are also characterized by the presence of Wark–Lovering (WL) rims. These rims are composed of

* Corresponding author. Address: Department of Earth and Space Science, 3806 Geology Building, 595 Charles E. Young Dr. East, Los Angeles, CA 90095, United States. Tel.: +1 310 592 0750.
E-mail address: katie.dyl@gmail.com (K.A. Dyl).

largely monomineralic bands (in some cases, bands of 2 or 3 minerals) that become increasingly Mg- and Si-rich towards the matrix enveloping the CAIs. A common sequence from the CAI interior outwards is spinel (\pm hibonite), melilite, Ti-bearing pyroxene, Al-rich pyroxene, and an outermost band of forsterite olivine (Wark and Lovering, 1977). CAIs from many carbonaceous chondrite groups have this feature, suggesting that WL rims all formed in a similar environment by a similar process. Wark and Lovering originally suggested a condensation origin for the rims. A condensation provenance is supported by low $^{25}\text{Mg}/^{24}\text{Mg}$ of rims, including spinel. These low Mg isotope ratios are indistinguishable from the matrix (Fahey et al., 1987) or slightly lower than matrix ratios (Simon et al., 2005), precluding evaporation but consistent with condensation. There are no reports of elevated values that result from evaporation, a fact that remains true even when the host CAI exhibits high $^{25}\text{Mg}/^{24}\text{Mg}$.

Later work suggested evaporation and metasomatism in a gaseous reservoir as a mechanism to form WL rims, with particular attention paid to the spinel-rich inner layer (MacPherson et al., 1981; Murrell and Burnett, 1987). The rare earth elements (REEs) in perovskite found in both CAIs and the spinel-rich inner layer of their WL rims both exhibit Group II patterns (i.e. depleted in refractory REEs). However, in the case of the rims it is unclear whether this REE pattern resulted from condensation from a reservoir that is depleted in refractory REEs or if instead the composition was inherited from the CAI itself (Murrell and Burnett, 1987). Ruzicka et al. modeled rim growth as the product of evaporation and diffusive metasomatism in the nebula driven by large chemical potential gradients between the host CAI and gas (Ruzicka, 1997). He showed that the mono- and poly-mineralic banding observed in Wark–Lovering rims, specifically between layers of spinel and clinopyroxenes, could form by metasomatic growth. This model fails to predict the formation of melilite, however, which is commonly observed in many CAI rims.

Simon et al. (2005) proposed a mechanism for WL rim formation based on ^{26}Al chronology, stable magnesium isotope ratios, and equilibrium phase relationships in the Ca–Mg–Al–Si–O system. The magnesium isotopic data and thermodynamic calculations are consistent with condensation of monomineralic bands driven by large chemical potential gradients (e.g., μ_{Si} , μ_{Mg}) at the CAI–gas interface. In this scenario, these large μ gradients were imposed as CAIs experienced heating in a gas with relatively high magnesium, silicon, and oxygen partial pressures (P_{Mg} , P_{SiO} , P_{O_2}). The result was growth of successive melilite, Al-rich pyroxene, diopside, and forsterite bands. The chronological constraints from the Al–Mg chronometer indicate that this processing occurred $\leq 300,000$ years after CAI formation (Simon et al., 2005).

Simon et al. (2005) showed that titanium valence in the WL rim of Leoville 144A, the type A compact CAI studied (Fig. 1), was more oxidized than in the interior of the CAI. The $\text{Ti}^{3+}/\text{Ti}^{4+}$ ratios for the interior and rim of 144A were obtained from charge balance based on cation norms from electron microprobe analyzer (EMPA) data. Most analyses of Al, Ti-rich pyroxene in the WL rim of Leoville 144A have no detectable Ti^{3+} , while two other areas have $\text{Ti}^{3+}/$

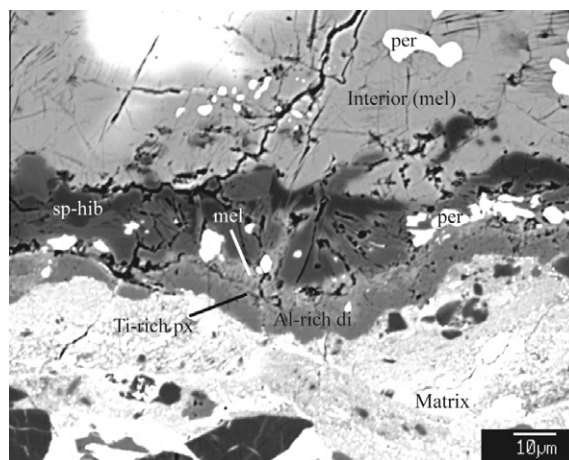


Fig. 1. BSE image of Leoville 144A Wark–Lovering rim. Bands of spinel + hibonite \pm perovskite (sp-hib, pv), melilite (mel), Al-Ti diopside (Ti-rich px), and Al-diopside (Al-di) are observed.

Ti^{4+} ratios of ~ 1 (Dyl et al., 2005). These $\text{Ti}^{3+}/\text{Ti}^{4+}$ values are substantially lower than the $\text{Ti}^{3+}/\text{Ti}^{4+} \sim 2$ that characterizes pyroxenes of the CAI interior. These findings support the petrologic evidence for an increase in P_{O_2} during rim formation. They also argue against evaporation as the sole formation mechanism of WL rims and are inconsistent with metasomatic reactions that do not include oxidation as a process occurring in the vapor phase.

Recent work by Simon et al. (2009) interpreted the reported EMPA estimates of $\text{Ti}^{3+}/\text{Ti}^{4+}$ in the rim of Leoville 144A by Simon et al. (2005) as analytical artifacts (Simon et al., 2007). The former authors developed a XANES technique to determine titanium valence state in pyroxene. They applied their technique to sample 144A at eight different rim sites located at varying distances from the CAI interior. XANES measurements suggest higher Ti^{3+} abundances in the WL rim of 144A, with $\text{Ti}^{3+}/\text{Ti}^{4+}$ ratios as high as 2.4 reported. The XANES measured $\text{Ti}^{3+}/\text{Ti}^{4+}$ range from -0.06 to 2.44 (corresponding to $\text{Ti}^{3+}/\text{Ti}_{\text{total}} = -0.06$ to 0.71). Averages for each rim region give $\text{Ti}^{3+}/\text{Ti}^{4+}$ ratios from 0.32 to 1.08 ($\text{Ti}^{3+}/\text{Ti}_{\text{total}} = 0.1$ – 0.52). For this reason Simon et al. re-interpreted the electron microprobe data of Simon et al. (2005) as X-ray contamination from neighboring phases. They suggested that spinel contamination occurred based on the higher Al content, cation excess, and $\text{Ca} < 1.00$ per formula unit (pfu) for EMPA analyses of WL rim pyroxenes. Alteration was also suggested as a possible explanation for the EMPA results.

To investigate these claims, we re-analyzed Leoville 144A to obtain a more complete set of $\text{Ti}^{3+}/\text{Ti}^{4+}$ values in the Wark–Lovering rim and compared our new results with those of Simon et al. The WL rim of another CAI, Ef3, was also measured via EMPA to characterize Ti valence states in another object. The distinctly different petrography of this object is observed in Fig. 2. We also conducted experiments on spinel–pyroxene overlap during EMPA analysis to quantify the consequences of X-ray mixing. We use these data to evaluate the plausibility of spinel–mixing in WL rim pyroxene analyses.

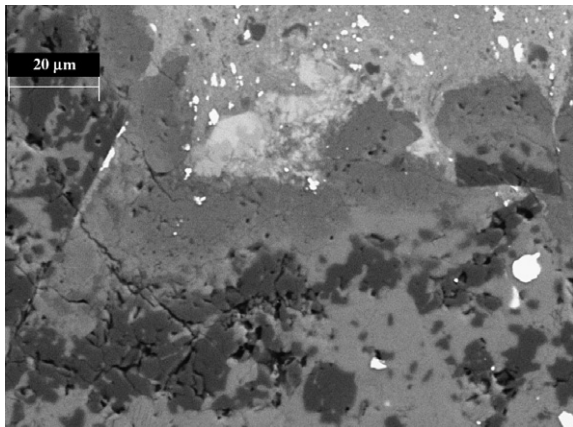


Fig. 2. BSE image of Ef3. Bands of spinel \pm melilite (sp–mel), spinel \pm Al–Ti diopside (sp, Ti–px), and Al–diopside (Al–di) are observed.

While we find a wider range of $\text{Ti}^{3+}/\text{Ti}^{4+}$ in these WL rims as a result of our more exhaustive search for suitable analysis sites, we reaffirm our original conclusion: WL rim and CAI interior pyroxenes are compositionally distinct, with $\text{Ti}^{3+}/\text{Ti}^{4+}$ lower in the rim. We show that both EPMA and XANES data support this statement, and spinel–mixing cannot explain the observed differences in valence states obtained by EPMA. We reassert, therefore, that WL rim pyroxenes record evidence of a more oxidizing environment during their formation than that during formation of CAIs themselves.

2. ANALYTICAL METHODS

All electron microprobe analyses were obtained with the UCLA JEOL Superprobe using a focused electron beam. The electron beam current was 15 nA with an accelerating voltage of 15 kV. Abundances of Ti^{3+} and Ti^{4+} were calculated assuming a cation:oxygen ratio of 4:6 and no cation vacancies. The absence of any other major element with more than one valence state (e.g., Fe) facilitates the application of cation norms for this purpose. The code containing the algorithm used to calculate Ti^{3+} and Ti^{4+} concentrations in the pyroxenes is given in the [Electronic Annex](#). The equilibria defining $f\text{O}_2$ using the oxidation state of Ti in the pyroxenes were discussed in depth in our previous work (Simon et al., 2005). In some instances (one analysis in the present study), negative values for Ti^{3+} per formula unit can result where errors in cation abundances exceed the discrepancy in charge balance incurred by assuming all Ti is Ti^{4+} . We have chosen to allow the recalculation scheme to permit negative values in these instances as a measure of the quality of analysis. Such values are understood to mean that the data do not support the presence of Ti^{3+} .

Simon et al. suggested that all analyses of calcic pyroxenes from CAIs should be normalized to 1.00 Ca pfu. While it is true that interior Ti-rich pyroxenes from CAI interiors tend to have 1 Ca pfu, we note that this characteristic is not typical of calcic pyroxenes in general. Indeed, we expect the

higher activity of Mg predicted during WL rim formation would promote a departure from the diopside–hedenbergite join into the augite field of the pyroxene quadrilateral (e.g., augite is defined as having Ca < 1 per 6 oxygen). For this reason we do not normalize our pyroxene analyses to 1.00 Ca pfu.

We augmented the data set for WL rim pyroxenes in Leoville 144A presented by Simon et al. (2005) (Dyl et al., 2008). Whereas we used Ti maps produced by EMPA in our first study to choose analysis sites, we relied solely on backscattered electron (BSE) images to locate the most Ti-rich pyroxenes in the rim in our follow-up work. We also analyzed Ti-rich pyroxene in the WL rim of Ef3, a compact-Type A CAI from CV3 Efremovka, to explore the Ti^{3+} -content in other CAIs via EMPA.

In order to quantify the potential effects of mixing characteristic X-rays from adjacent spinel and pyroxene during analysis, we collected EMPA measurements along eight traverses in the interior of Leoville 144A extending from spinel into neighboring fassaite. Elemental compositions were obtained at 0.5 μm intervals along traverses perpendicular to the spinel–fassaite phase boundaries. The electron beam activation diameter is on the order of 2 μm at our operating conditions (see Sections 3 and 4).

3. RESULTS

3.1. WL rim pyroxene in Leoville 144A

Titanium concentrations in the five new analyses of WL rim pyroxene from 144A range from 5% to 8% by weight as TiO_2 . This is within the range of the more Ti-rich pyroxenes analyzed previously. Calcium per formula unit for these pyroxenes ranges from 0.94 to 0.96 and also consistent with previous analyses. All five new analyses show discernable Ti^{3+} . The additional $\text{Ti}^{3+}/\text{Ti}^{4+}$ ratios overlap with our previous analyses with $4 < 1$; one analysis has $\text{Ti}^{3+}/\text{Ti}^{4+} > 1$, but still lower than the ratio observed in the interior of Leoville 144A. New WL pyroxene elemental compositions are compiled in Table 1, as are representative analyses previously presented by Simon et al. (2005).

3.2. Spinel–pyroxene traverses in Leoville 144A

The spinel–pyroxene traverses rule out cross-contamination of mineral analyses by EMPA at distances greater than 1.5 μm from the phase boundary. Fig. 3 illustrates the correlation between measured pyroxene Ca pfu and Ti^{3+} pfu versus distance within 1.5 μm of the phase boundary. All measurements in this close proximity to the phase boundary fall on calculated mixing lines between spinel and the interior CAI pyroxene. At a distance of 1 μm from the phase boundary, roughly 5% of the analyzed material corresponds to spinel. At a distance of 1.5 μm , the analyses show no contamination from adjacent spinel grains. We conclude that spinel must be within 1.5 μm of a pyroxene analysis spot in order to impact the pyroxene analysis. We see no evidence for X-ray fluorescence effects, which would cause the electron microprobe analyses to deviate from the theoretical mixing trend. Analyses directly on the phase bound-

Table 1

New EMPA analyses of WL rim pyroxenes in Leoville 144A, with previously reported interior Ti-rich pyroxene and WL rim pyroxene (a) for comparison (Simon et al., 2005). 1σ is determined from Monte Carlo error analysis.

Analysis	WL rim 1		WL rim 2		WL rim 3		WL rim 4		WL rim 5		Interior		WL Rim (2005) ^a	
	Wt %	Cations	Wt %	Cations	Wt %	Cations	Wt %	Cations	Wt %	Cations	Wt %	Cations	Wt %	Cations
<i>EMPA analyses and cations assuming 6 oxygen</i>														
SiO ₂	42.0881.522		43.0351.574		40.1691.467		41.9741.53		42.5791.544		34.2031.27		38.3961.393	
Al ₂ O ₃	14.4630.617		12.8330.553		17.0090.732		15.0220.646		15.5840.666		17.3930.761		20.0270.856	
TiO ₂	7.6570.208		6.3690.175		7.1330.196		5.8830.161		5.0550.138		15.8490.443		5.8310.159	
FeO	0.8650.026		1.2390.038		1.1080.034		1.4050.043		0.9570.029		0.0380.001		1.0180.031	
Cr ₂ O ₃	0.2030.006		0.2120.006		0.1360.004		0.1170.003		0.1350.004		0.0520.002		0.2 0.006	
MnO	0 0		0.0050		0 0		0.0040		0 0		0 0		0 0	
MgO	11.7470.633		12.28 0.669		10.8570.591		12.2510.666		11.8850.643		8.2240.455		12.4750.675	
CaO	24.3790.945		24.3890.955		24.0360.941		23.8440.932		24.5670.955		24.4660.973		23.0760.897	
Na ₂ O	0.04 0.003		0.01 0.001		0.0340.002		0.0550.004		0.0990.007		0.0150.001		0.0170.001	
K ₂ O	0.01 0		0.0210.001		0.0580.003		0.0180.001		0.0060		0.0150.001		0 0	
Total	101.4523.96		100.3933.973		100.54 3.971		100.5733.986		100.8673.986		100.2553.907		101.04 4.018	
Analysis	WL rim 1		WL rim 2		WL rim 3		WL rim 4		WL rim 5		Interior		WL rim (2005) ^a	
	Cations	1σ	Cations	1σ	Cations	1σ	Cations	1σ	Cations	1σ	Cations	1σ	Cations	1σ
<i>Recalculated to 4 cations per 6 oxygen (Ti³⁺ present)</i>														
Si	1.537	0.004	1.584	0.004	1.478	0.004	1.536	0.004	1.55	0.004	1.3	0.004	1.387	0.004
Al	0.623	0.003	0.557	0.003	0.738	0.003	0.648	0.003	0.669	0.003	0.779	0.003	0.853	0.003
Ti ⁴⁺	0.089	0.007	0.093	0.007	0.11	0.009	0.12	0.007	0.097	0.007	0.167	0.007	0.211	0.007
Ti ³⁺	0.121	0.008	0.083	0.008	0.088	0.009	0.042	0.008	0.042	0.007	0.286	0.008	−0.053	0.007
Fe	0.027	0.001	0.038	0.001	0.034	0.001	0.043	0.001	0.029	0.001	0.001	0.001	0.031	0.001
Cr	0.006	0.001	0.006	0.001	0.004	0.001	0.003	0.001	0.004	0.001	0.001	0.001	0.006	0.001
Mn	0	0	0	0	0	0	0	0.001	0	0	0	0	0	0
Mg	0.64	0.003	0.674	0.003	0.596	0.003	0.668	0.003	0.645	0.003	0.466	0.003	0.672	0.003
Ca	0.954	0.003	0.962	0.003	0.948	0.003	0.935	0.003	0.958	0.003	0.997	0.003	0.893	0.003
Na	0.003	0.001	0.001	0.001	0.002	0.001	0.004	0.001	0.007	0.001	0.001	0.001	0.001	0.001
K	0	0	0.001	0.001	0.003	0.003	0.001	0.001	0	0	0.001	0.001	0	0
Ti ³⁺ /Ti ⁴⁺	1.369	0.196	0.899	0.151	0.812	0.151	0.356	0.085	0.438	0.109	1.716	0.118	−0.248	0.026
Ti ³⁺ /Ti _{total}	0.575	0.034	0.47	0.041	0.444	0.045	0.26	0.046	0.301	0.052	0.631	0.016	−0.332	0.046

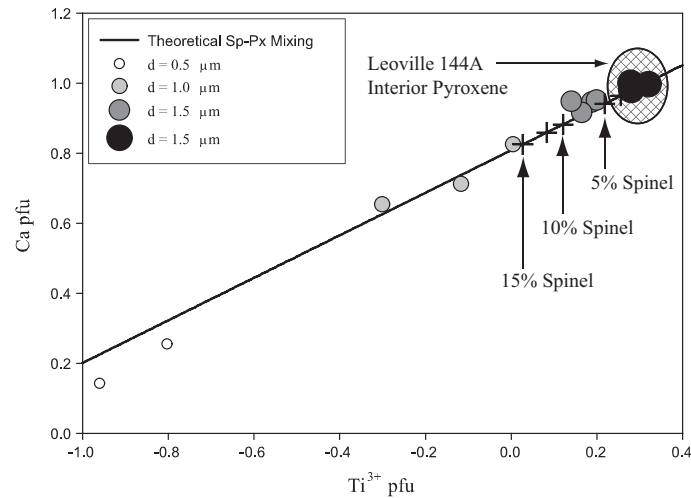


Fig. 3. Traverses across spinel–pyroxene interface plotted and compared to a calculated mixing line between the two phases. Traverse data are represented by circles; size and color signify distance from the spinel–pyroxene interface. The solid line corresponds to the theoretical mixing trend between Ti-rich pyroxene and spinel. Leoville 144A interior compositions from Simon et al. (2005) plot within the shaded area. This illustrates that a distance $<1.5 \mu\text{m}$ from spinel is required for phase contamination.

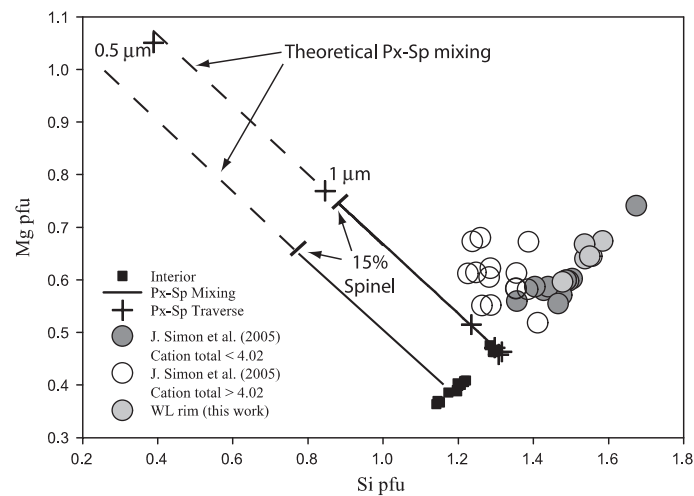


Fig. 4. Ti-rich pyroxene data for Leoville 144A plotted in the element space Mg vs. Si. Spinel–pyroxene traverses plot on a trend consistent with mixing. WL rim pyroxene data with cation totals <4.02 pfu are inconsistent with this trend, with both Mg and Si contents are increasing. Cation totals >4.02 pfu requires as much as 15% spinel, requiring a distance $>1.5 \mu\text{m}$ from spinel grains.

ary are the only exception; they show a deviation from the theoretical mixing trend.

Simon et al. used bivariate plots of Ca pfu and Al pfu versus cation totals to argue for contamination of pyroxene analyses by spinel, showing that the WL rim pyroxenes plotted along the theoretical mixing line between spinel and pyroxene (Simon et al., 2007). If correct, spinel–pyroxene mixing should be evident in all relevant composition spaces. We compared our Leoville 144A pyroxene data to our spinel–pyroxene traverses and theoretical mixing trends in a variety of relevant multi-element spaces to test this hypothesis that the WL pyroxene data are “polluted” by X-rays from nearby mineral phases. Fig. 4 illustrates that the correlation representing spinel–pyroxene mixing is not seen in Mg versus Si space. Three different data sets ob-

tained for Leoville 144A are shown in Fig. 4: analyses from Simon et al. (2005) with cation totals less than 4.02 per 6 oxygen (dark grey circles), analyses with greater than 4.02 cations pfu (white), and new analyses from this study (black). The addition of spinel results in a negative slope in Mg/Si space due to spinel contamination while WL rim pyroxenes from 144A define a trend orthogonal to the spinel–pyroxene mixing. Pyroxenes with cation totals >4.02 pfu would require as much as 15% spinel contamination to explain their excess cations as the result of spinel pollution. This is highly unlikely, given that 15% contamination would be observed less than $0.5 \mu\text{m}$ away from spinel grains in the interior (Fig. 3), and none of our pyroxene data were obtained closer than $8 \mu\text{m}$ to spinel. None of these analyses contain 1 Ca pfu.

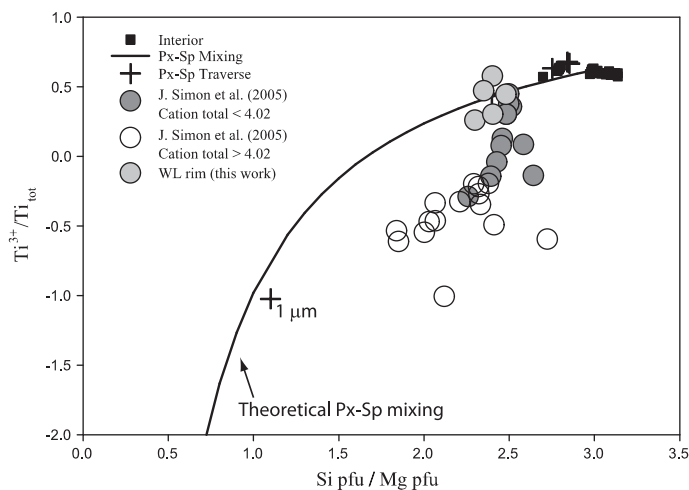


Fig. 5. Pyroxene EMPA data for Leoville 144A plotted in the space Ti^{3+}/Ti_{tot} vs. Si/Mg. The measured spinel–pyroxene (sp–px) mixtures fall along a calculated spinel–pyroxene mixing curve. Wark–Lovering rim pyroxenes exhibit a trend very different from sp–px mixing.

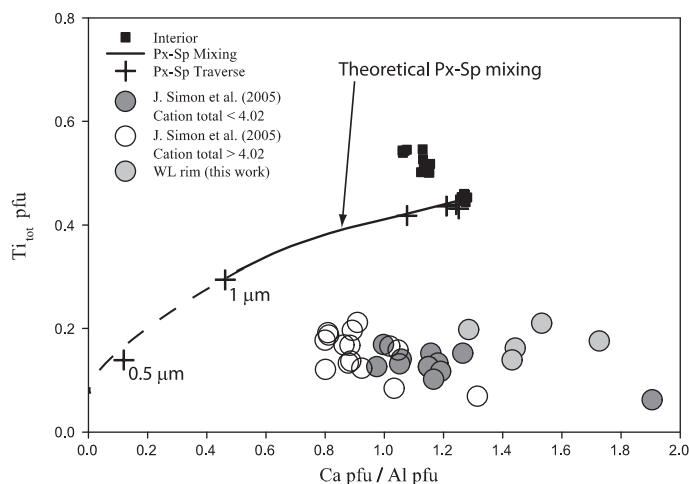


Fig. 6. Pyroxene data for Leoville 144A plotted in the element space Ca/Al vs. Ti_{tot} . Measured spinel–pyroxene mixing traverses match the theoretical mixing trend between the two phases in this space. Wark–Lovering rim pyroxene data show no discernable trend. Interior pyroxenes also contain more total titanium in their structures.

Another symptom of spinel contamination is that Ti^{3+} pfu values obtained by charge balance are lowered due to the fact that spinel has a higher cation-to-oxygen ratio of 3:4 compared with 2:3 for pyroxene. Fig. 5 compares this effect against our pyroxene data in (Ti^{3+}/Ti_{total}) versus Si/Mg space. Increasing spinel contributions decrease the Si/Mg ratio to a greater extent than does Ti^{3+} , as shown by the black curve. This results from the relatively small difference in the cation to oxygen ratio of the two phases. The spinel–pyroxene traverse data fall on the predicted spinel–pyroxene mixing trend. Wark–Lovering rim pyroxenes, on the other hand, display a distinctly different trend that is independent of cation totals. Whereas spinel–pyroxene mixing results in a concave slope in Fig. 5, WL analyses display a convex pattern (with the exception of ~ 5 analyses).

In Fig. 6 we show Ca/Al ratios plotted against total Ti contents in pyroxenes. We expect aluminum to increase with spinel contamination, with accompanying decreases

in both Ca and Ti. Here again the WL rim data deviate from the expected spinel–pyroxene mixing trend while the traverses across the spinel–pyroxene phase boundary adhere to the mixing trend.

We considered contamination from other phases in the EMPA analyses, ruling them out as well. Melilite is an adjacent phase in several cases, but contamination by melilite would increase, rather than decrease, the concentration of calcium. Contamination from Al-diopside would have a negligible effect, and would only manifest itself as lower titanium abundance. Simon et al. refer to the possibility of unseen olivine contamination to explain the presence of Fe; we observe no evidence for proximal olivine.

3.3. Comparison to Ef3 WL rim pyroxene

We obtained 37 individual analyses of Ti-rich pyroxene in the WL rim of Ef3 with TiO_2 ranging from 4.8% to

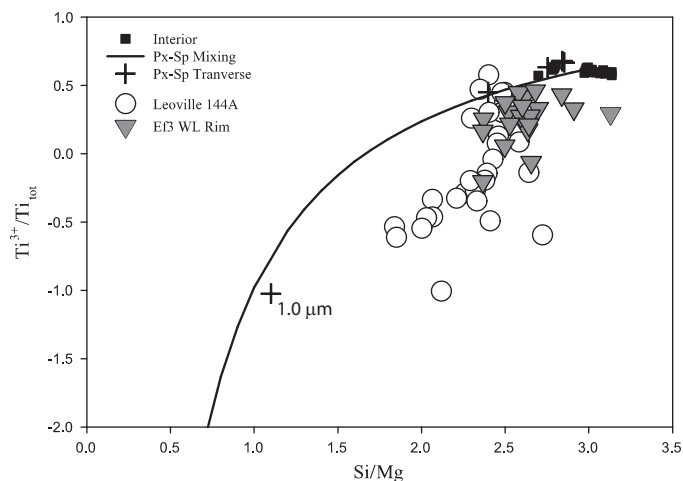


Fig. 7. Wark–Lovering rim data from compact-Type A CAI Ef3 (grey triangles) plotted as $\text{Ti}^{3+}/\text{Ti}_{\text{tot}}$ versus Mg/Si. Leoville 144A WL rim data (white circles) are plotted as well. Both data sets show the same major element trend. This trend is inconsistent with spinel mixing, but is consistent with formation in an environment of greater partial pressure of Mg ($\text{Mg}_{(g)}$) compared with the environment for CAI formation.

11.0% by weight. All analyses are from the WL rim of Ef3; however, there are two petrographic settings for Ti-rich pyroxene in this object. Pyroxene can be found associated with both the inner spinel layer and Al-rich diopside. The first occurrence of Ti-rich pyroxene has $\text{Ti}^{3+}/\text{Ti}^{4+}$ values around 1.5, consistent with interior CAI values. Our analyses discussed here are of pyroxene we believe to be associated with the outer diopside layer. Fourteen analyses in the rims have $\text{Ti}^{3+}/\text{Ti}^{4+} > 1$, making them indistinguishable from CAI interior Ti-rich pyroxene. Twenty two analyses display $\text{Ti}^{3+}/\text{Ti}^{4+}$ ranging from 0.06 to 0.89. One analysis contains no discernable Ti^{3+} ; the cation total of the raw EMPA analysis is 4.0 cations per 6 oxygen. All pyroxenes analyzed have Ca pfu from 0.93 to 0.99 and exhibit no correlation between Ti^{3+} content and Ca pfu.

Electron microprobe analyses of pyroxenes from WL rims from both 144A and Ef3 follow similar trends. For example, Fig. 7 shows a plot of $\text{Ti}^{3+}/\text{Ti}_{\text{total}}$ versus Mg/Si for Ti-rich pyroxene in Ef3 with $\text{Ti}^{3+}/\text{Ti}^{4+} < 1$ (analyses comparable to the interior are excluded) compared with WL rim data from Leoville 144A. The data from the rims of these two CAIs overlap and are distinct from the spinel–pyroxene mixing trend.

4. DISCUSSION

4.1. Valence state of Ti in the WL rim of Leoville 144A

The comparison between our augmented data set, the XANES data, and the interior Ti-rich pyroxene (interior pyroxene $\text{Ti}^{3+}/\text{Ti}^{4+}$ are not in dispute) reveals that there is a distinct difference in $\text{Ti}^{3+}/\text{Ti}^{4+}$ between WL rim and interior pyroxenes using electron microprobe estimates and/or XANES (Simon et al., 2005, 2007). Fig. 8 shows a probability density plot of all Ti-bearing pyroxene analyses for Leoville 144A. While XANES, and the additional electron microprobe analyses, show that Ti^{3+} is present in Wark–Lovering rims, they also show that $\text{Ti}^{3+}/\text{Ti}_{\text{total}}$ is markedly lower in the WL rim than in the interior of the CAI.

Simon et al. (2007) report additional electron microprobe data that also support this conclusion. They measured 10 WL rim pyroxenes containing >4 wt% TiO_2 . Among these, five have no discernable Ti^{3+} ; five have $\text{Ti}^{3+}/\text{Ti}_{\text{total}}$ ratios that range from 0.18 to 0.83, with an average of 0.42 ± 0.26 when normalizing to 4 cations pfu as compared with $\text{Ti}^{3+}/\text{Ti}_{\text{total}} \sim 2/3$ (expressed as $\text{Ti}^{3+}/\text{Ti}^{4+}$ ratio, WL rim analyses have an average of 0.72 compared to ~ 1.5 for interior Ti-rich pyroxene) for the interior pyroxenes. While several of their analyses show Ti^{3+} values $>50\%$ of total Ti, in contrast to our observations, the average $\text{Ti}^{3+}/\text{Ti}^{4+}$ of the WL rim pyroxenes is consistent with our data.

XANES analyses show a similar trend. Of the 10 WL rim pyroxenes analyzed, Simon et al. indicated that only the six of those showing the highest $\text{Ti}^{3+}/\text{Ti}_{\text{total}}$ could be reliably interpreted as pyroxene analyses (an issue due to the large activation region of the XANES spots relative to the size of the WL rims). The average $\text{Ti}^{3+}/\text{Ti}_{\text{total}}$ for these areas ranged from 0.33 to 0.52, considerably lower than the ≥ 0.65 for the pyroxene in the interior of the CAI. While several analyses are outside the range of reported electron microprobe values, the average $\text{Ti}^{3+}/\text{Ti}_{\text{total}}$ of each rim area is clearly distinguishable from interior Ti-bearing pyroxene values. The two areas analyzed by XANES that showed little to no Ti^{3+} were excluded due to potential analytical artifacts; one area had a rim thickness of ~ 10 μm , on par with the depth of XANES analyses, and thus was likely contaminated by matrix. Another was thought to be contaminated by Ti- and Fe-bearing alteration products (Simon et al., 2007).

The EMPA data obtained for the WL rim of Leoville 144A appear to have a bimodal distribution of Ti^{3+} contents. Previously published analyses are largely devoid of Ti^{3+} while XANES, as well as our new analyses, peak at $\text{Ti}^{3+}/\text{Ti}^{4+} \sim 0.5$. We believe this difference is due to how we identified Ti-rich pyroxenes to analyze. In previous work, we used X-ray Ti maps to locate Ti-rich pyroxene in the WL rim. We used BSE contrast differences in the

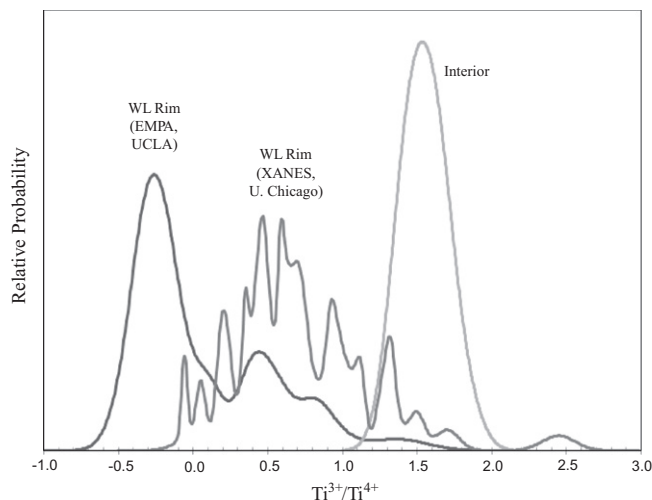


Fig. 8. Probability density plot showing all measurements of titanium valence state in Leoville 144A. Estimated errors of 0.3 pfu are used to construct the curves for the EMPA data, and reported uncertainties are used to construct the probability function for XANES data (Simon et al., 2005, 2007).

analyses reported here. Titanium-rich pyroxene with higher Ti^{3+}/Ti^{4+} values appear lighter in BSE imaging, presumably due to a lower enstatite component. Our goal was not to obtain a representative distribution of Ti^{3+} in WL rim pyroxene. We sought to verify our previous assertion that WL rim Ti^{3+} values were distinct and lower than those found in CAI interiors. A more complete survey is required to better define the distribution of Ti^{3+} -bearing and Ti^{3+} -absent pyroxene in Leoville 144A.

In summary, both techniques yield a wide range of Ti^{3+}/Ti_{total} values for the WL rim. Pyroxenes with no Ti^{3+} are obtained by both methods, albeit with varying degrees of reliability. Further work will be required to elucidate any relationships between petrography and the oxidation state of rim formation that may exist. It is clear, however, that the formation of WL rims occurred under more oxidizing conditions than those that accompanied the formation of interior Al-Ti-pyroxene.

4.2. Titanium valence state of WL rims from Ef3

There are distinct petrographic differences between rims in 144A and those in Ef3. We suggest that such differences may correlate with the nebular conditions experienced by different CAIs during WL rim formation. The Ti-rich WL rim pyroxenes analyzed in Ef3 display Ti^{3+} contents comparable to the CAI interior, as well as a population of more oxidized compositions. Whereas Leoville 144A has a continuous, well-defined rim of spinel + hibonite + perovskite adjacent to the CAI, Ef3 grades from melilite into spinel (see Fig. 2). Ti-rich pyroxene is found intergrown with spinel in Ef3 rims, representing another stark difference from Leoville 144A. In the later case, where we see more oxidized Ti contents, the spinel layer is not adjacent to the Ti-rich pyroxene. In some areas of Ef3, the WL rim appears discontinuous, and Al-diopside is found adjacent the CAI interior.

4.3. Understanding compositional variations between interior and WL rim pyroxene

These new data show that spinel contamination cannot account for the elemental correlations observed in WL rim pyroxenes. All EMPA analyses of WL rim pyroxenes are greater than 8 μm away from the spinel/hibonite layer, more than four times the diameter of the activation volume of the electron beam (Simon et al., 2005). Contributions from spinel below the sample surface would require the innermost spinel–hibonite band to have an angle of 10° relative to the section surface, assuming all mineral bands do not vary significantly in thickness as a function of depth. This is ruled out because the rims can be observed on the underside of the $\sim 30 \mu m$ thick sample, precluding such an extreme geometry.

We invoke crystal chemical closure effects to explain major element trends in WL rim pyroxenes. Less calcium in the pyroxene M2 site is a consequence of less Ca present in the rim-forming environment. Magnesium is thus incorporated into the M2 site to replace Ca. The consequence is that these pyroxenes resemble many terrestrial calcic pyroxenes in having Ca and Mg occupying the M2 site.

This conclusion is illustrated by recalculating our pyroxene compositions in terms of moles of pyroxene components. Table 2 lists the proportions of pyroxene components in Leoville 144A interior and WL rim pyroxenes. The components considered are: $CaAl_2SiO_6$ (Ca-Tschermak, CaTs), $CaTi^{3+}AlSiO_6$ (T3), $CaT^{4+}Al_2O_6$ (T4), $CaMgSi_2O_6$ (diopside di/Di), $Mg_2Si_2O_6$ (enstatite, en), and $Fe_2Si_2O_6$ (ferrosilite, fs). Uncorrected cation totals for Si, Al, Ca, Ti, Mg, and Fe were transformed into these components using linear algebra techniques (Thompson, 1982a). In this process, pyroxene analyses in terms of cations per formula unit are transformed to a coordinate system composed of pyroxene endmember components. The transformation of components is afforded by the relation:

Table 2

Compositional analyses of Leoville 144A interior and WL rim pyroxenes. Cation totals reported in Table 1 are used; Ti (total) was used as a component instead of Ti^{3+} and Ti^{4+} individually. Pyroxene components are defined in the text. Interior and WL rim data denoted “spot” are taken from Simon et al. (2005) (Supplementary data).

	WL rim 1	WL rim 2	WL rim 3	WL rim 4	WL rim 5	Interior 32	Interior 40
CaAl ₂ SiO ₆	0.16	0.15	0.22	0.19	0.22	0.09	0.08
CaTi ³⁺ AlSiO ₆	0.13	0.09	0.10	0.05	0.06	0.34	0.29
CaTi ⁴⁺ Al ₂ O ₆	0.08	0.09	0.10	0.11	0.08	0.21	0.16
CaMgSi ₂ O ₆	0.58	0.64	0.53	0.59	0.60	0.36	0.46
Mg ₂ Si ₂ O ₆	0.03	0.02	0.03	0.04	0.03	0.00	0.00
Fe ₂ Si ₂ O ₆	0.01	0.02	0.02	0.02	0.01	0.00	0.00
Total	1.00	1.00	1.00	1.00	1.00	1.00	1.00

	WL rim spot 2	WL rim spot 4	WL rim spot 10	WL rim spot 15	WL rim spot 16	WL rim spot 19	WL rim spot 20	WL rim spot 25	WL rim spot 29
CaAl ₂ SiO ₆	0.30	0.28	0.26	0.32	0.31	0.30	0.29	0.31	0.36
CaTi ³⁺ AlSiO ₆	0.00	-0.03	-0.05	-0.01	0.05	0.01	0.06	0.03	-0.01
CaTi ⁴⁺ Al ₂ O ₆	0.17	0.24	0.21	0.11	0.08	0.11	0.08	0.11	0.13
CaMgSi ₂ O ₆	0.47	0.43	0.49	0.57	0.51	0.57	0.52	0.48	0.41
Mg ₂ Si ₂ O ₆	0.05	0.06	0.06	-0.01	0.05	0.00	0.04	0.05	0.08
Fe ₂ Si ₂ O ₆	0.02	0.02	0.02	0.02	0.02	0.01	0.02	0.01	0.02
Total	1.00	1.00	1.00	1.00	1.00	1.00	1.00	1.00	1.00

$$\begin{bmatrix} \text{Si pfu} \\ \text{Al pfu} \\ \text{Ti pfu} \\ \text{Ca pfu} \\ \text{Mg pfu} \\ \text{Fe pfu} \end{bmatrix} = \begin{bmatrix} 1 & 2 & 0 & 1 & 0 & 0 \\ 1 & 1 & 1 & 1 & 0 & 0 \\ 0 & 2 & 1 & 1 & 1 & 0 \\ 2 & 0 & 0 & 1 & 1 & 0 \\ 2 & 0 & 0 & 0 & 2 & 0 \\ 2 & 0 & 0 & 0 & 0 & 2 \end{bmatrix} \times \begin{bmatrix} \text{CaTs} \\ \text{T3} \\ \text{T4} \\ \text{di} \\ \text{en} \\ \text{fs} \end{bmatrix}^T \quad (1)$$

Eq. (1) corresponds to $Y=AX$, where A is the coefficient matrix, X is the vector containing moles of components comprising each analysis, and Y is the vector of cations per formula unit. Solving for the moles of components by inverting A , such that $X=A^{-1}Y$, we have

$$\begin{bmatrix} 0.5 & 1 & -1 & -0.5 & 0.25 & 0 \\ 0.5 & 0 & 0 & -0.5 & 0.25 & 0 \\ -0.5 & 1 & 0 & -0.5 & 0.25 & 0 \\ -0.5 & -1 & 1 & 1.5 & -0.75 & 0 \\ -0.5 & -1 & 1 & 0.5 & 0.25 & 0 \\ -0.5 & -1 & 1 & 0.5 & -0.25 & 0.5 \end{bmatrix} \times \begin{bmatrix} \text{Si pfu} \\ \text{Al pfu} \\ \text{Ti pfu} \\ \text{Ca pfu} \\ \text{Mg pfu} \\ \text{Fe pfu} \end{bmatrix} = \begin{bmatrix} \text{CaTs} \\ \text{T3} \\ \text{T4} \\ \text{di} \\ \text{en} \\ \text{fs} \end{bmatrix}^T \quad (2)$$

In other words, by inverting the coefficient matrix in Eq. (1), we transform EMPA analyses into pyroxene components by Eq. (2). Only the four Ca-containing components are required to define the compositions of interior CAI pyroxenes. Wark–Lovering rim pyroxenes, however, cannot be represented in pyroxene composition space without the addition of an enstatite component. Ferrosilite is added as a minor component due to the presence of ~ 0.03 Fe pfu.

Wark–Lovering rim trends among major elements (Figs. 4–6) are also consistent with our hypothesized environment of rim formation. The trend in Fig. 4 results from both magnesium and silicon increasing in rim pyroxenes, as opposed to the silicon decrease predicted by spinel contamination. The convex mixing trend in Fig. 5 is also explained by increases in both elements, although magnesium

incorporation outstrips that of silicon (due to magnesium substitution in the M2 site). The absence of a trend between Ca/Al and titanium in Fig. 6 is further evidence that calcium and aluminum contamination are not responsible for compositional variations between interior and rim pyroxenes.

We note that most calcic pyroxenes, both terrestrial and extraterrestrial, do not have 1 Ca pfu. This suggests pyroxene in the interiors of CAIs have a rare composition that reflects their unique formation environment.

4.4. Reaction Space for CAI Pyroxene Evolution

Our hypothesis for WL rim formation can be tested by exploring the reactions between phases in an environment of elevated P_{Mg} , P_{Si} , and P_{O_2} . To do this, we constructed a reaction space to quantify how a CAI interior pyroxene composition evolves to WL rim compositions in an oxidizing solar nebula. This technique allows us to predict and quantify compositional effects that result from such an environment. A matrix of phase components defined in terms of system components describes how various elements can be distributed among the solid and gas phases comprising the system of interest (Thompson, 1982b):

$$\begin{array}{c} \text{SiO}_2 \text{ AlO}_{3/2} \text{ CaO} \text{ TiO}_{3/2} \text{ MgO} \text{ O} \\ \text{CaMgSi}_2\text{O}_6 \text{ (Di)} \\ [\text{Al}_2\text{Mg}_i\text{Si}_{-i}]_{\text{px}} \\ [\text{Ti}^{3+}\text{AlMg}_i\text{Si}_{-i}]_{\text{px}} \\ [\text{Ti}^{4+}\text{Al}_2\text{Mg}_i\text{Si}_{-2}]_{\text{px}} \\ [\text{MgCa}_{-1}]_{\text{px}} \\ \text{CaTi}^{4+}\text{O}_3 \\ \text{Mg}_{(\text{g})} \\ \text{Ca}_{(\text{g})} \\ \text{SiO}_{(\text{g})} \\ \text{O}_{(\text{g})} \end{array} \begin{bmatrix} 2 & 0 & 1 & 0 & 1 & 0 \\ -1 & 2 & 0 & 0 & -1 & 0 \\ -1 & 1 & 0 & 1 & -1 & 0 \\ -2 & 2 & 0 & 1 & -1 & 1/2 \\ 0 & 0 & -1 & 0 & 1 & 0 \\ 0 & 0 & 1 & 1 & 0 & 1/2 \\ 0 & 0 & 0 & 0 & 1 & -1 \\ 0 & 0 & 1 & 0 & 0 & -1 \\ 1 & 0 & 0 & 0 & 0 & -1 \\ 0 & 0 & 0 & 0 & 0 & 1 \end{bmatrix} \quad (3)$$

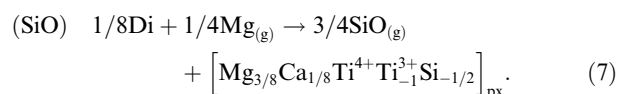
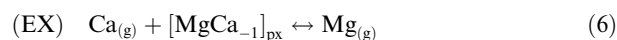
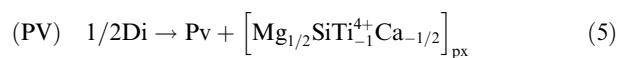
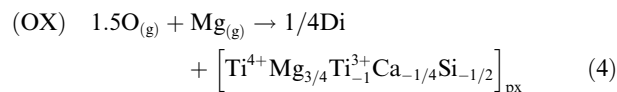
The coefficient matrix in Eq. (4) represents coefficients in the equations that define phase components in terms of trial system components. Row reduction of (3) to echelon form exposes the n linearly independent reactions that describe changes in mode and pyroxene composition in this system, where n is the difference between the number of phase components and the number of linearly independent system components. Using these reactions as axes of a reaction space, one can quantify the reaction pathway required to form WL rim pyroxene from CAI interior pyroxene as an initial composition. In so doing we assume the pyroxene in the WL rims are different from those in the interior by virtue of reactions between the CAI and the surrounding gas.

In the case of the reaction space where we wish to separate changes in modal abundances from changes in composition only, it is convenient to represent pyroxene compositions with a diopside additive phase component and four exchange components in Eq. (4) (see also Section 4.2). We emphasize that in constructing the reaction space we are not assuming CAI interior pyroxene itself is oxidized to form the WL rim; rather, we assume that the CAI interior pyroxene composition is representative of what a reducing nebula would condense. Iron was omitted for this analysis due to its negligible impact on the chemistry of interest. Additional phase components in (3) are $\text{Mg}_{(g)}$, $\text{Ca}_{(g)}$, $\text{SiO}_{(g)}$, and $\text{O}_{(g)}$ in the gas phase and perovskite.

Perovskite is included on the basis of petrographic and experimental evidence that it is a product of elevated Ti^{4+}

in the pyroxene structure. Perovskite is observed adjacent to pyroxene in the WL rim throughout Leoville 144A (Fig. 9), and previous work has shown that increasing the Ti^{4+} -content in the diopside- $\text{CaTi}^{4+}\text{Al}_2\text{O}_6$ binary system results in the formation of perovskite above 11 wt.% TiO_2 at $P = 1$ bar (Yagi and Onuma, 1967). All CAIs do not contain perovskite in their WL rim, and in such cases the phase components must be adjusted.

Row-reduction of the matrix in Eq. (3) results in the following 4 independent reactions that describe this system:



Reactions (4, OX) and (7, SiO) describe the oxidation of Ti^{3+} to Ti^{4+} . In (OX), oxygen and magnesium in the gas phase react to produce new pyroxene, and the composition of existing pyroxene increases in Ti^{4+} as an enstatite component is introduced at the expense of calcium. In (SiO), silicon, not oxygen, is the oxidant. $\text{SiO}_{(g)}$ is produced, and calcium contents of pyroxene increase. Reaction (5, PV) describes the formation of perovskite at the expense of pyroxene. This reaction also increases the enstatite component in

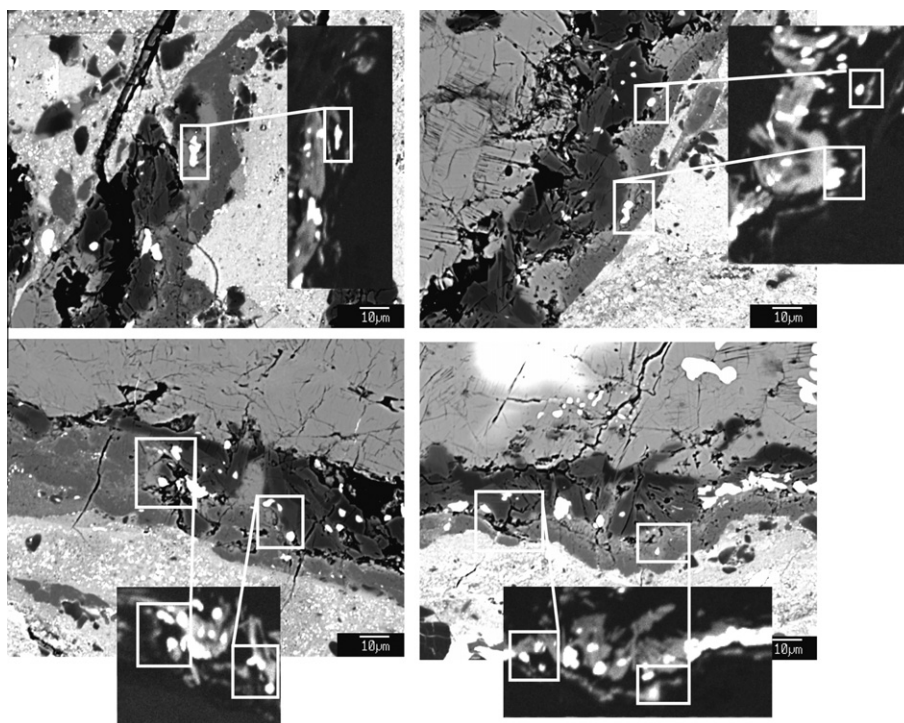


Fig. 9. Backscattered electron images of the WL rim of Leoville 144A and accompanying X-ray maps of titanium. All areas contain Ti-rich pyroxenes and perovskite (bright white phase) adjacent to pyroxene. White boxes correspond to areas containing perovskite adjacent to WL rim pyroxene. See Fig. 1 as well.

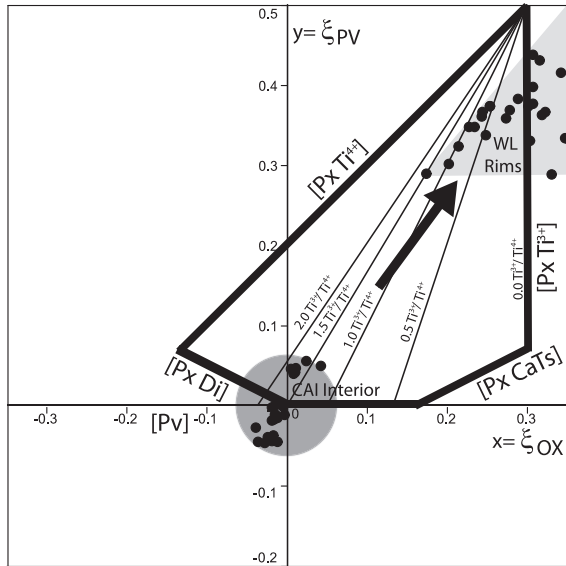


Fig. 10. Reaction space for CAI and WL rim pyroxenes. Coordinate axes (OX) and (PV) are defined in the text. Black dots correspond to interior CAI and WL rim pyroxene data from this study and previous work (Simon et al., 2005). The labeled shaded regions define the areas of reaction space occupied by the data for interiors and WL rims.

the pyroxene that remains, decreasing the concentrations of titanium and calcium in the pyroxene. Reaction (5, EX) is simply magnesium–calcium exchange between pyroxene and gas.

(OX) and (PV) can be used to define a two-dimensional reaction space for CAI and WL rim pyroxenes, depicted in Fig. 10. These reactions are chosen for this condensed space because they describe two dominant differences between

CAI interior and WL rim pyroxene: total titanium content and titanium oxidation state. The origin is defined by a representative CAI interior. Movement along the x -axis (OX) and the y -axis (PV) is measured by ξ_{OX} and ξ_{PV} , reaction progress in molar units. $\xi_{\text{OX}} = 0.3$ and $\xi_{\text{PV}} = 0.5$ correspond to the exhaustion of Ti^{3+} and total titanium in CAI interior pyroxene, respectively. Bold borders in reaction space delineate all boundaries where a phase or phase component is exhausted. The enclosed reaction space defines all possible pyroxene compositions that result from the oxidation of CAI interior pyroxene and perovskite formation.

EMPA analyses of Leoville 144A interior and its WL rim pyroxenes are plotted in reaction space using the calculated Ti^{3+} and Ti^{4+} abundances per formula unit. We obtain ξ_{OX} and ξ_{PV} for each datum using the following equations:

$$\xi_{\text{OX}} = \Delta \text{Ti}_{[\text{CAI-WL}]^{3+}} \quad (8)$$

$$\xi_{\text{PV}} = \Delta \text{Ti}_{\text{total} [\text{CAI-WL}]} \quad (9)$$

where [CAI-WL] denotes the difference between Leoville 144A interior pyroxene and WL rim pyroxene analyses and Ti refers to cations per formula unit.

Fig. 10 illustrates that WL rim pyroxene compositions are consistent with oxidation of Ti^{3+} and growth of perovskite. ξ_{OX} varies between 0.16 and 0.3; ξ_{PV} has a more narrow range of 0.3 to 0.4. Leoville 144A interior pyroxenes are also plotted and show the range of initial compositions observed. Solid lines show how the $\text{Ti}^{3+}/\text{Ti}^{4+}$ ratio varies as a function of both (OX) and (PV). Interior CAI pyroxenes show little deviation from the line defining $\text{Ti}^{3+}/\text{Ti}^{4+} = 1.5$. Wark–Lovering rim pyroxenes extend to the right of this line to the edge of reaction space defined by exhaustion of Ti^{3+} in pyroxene.

The reaction space in Fig. 10 also explains other compositional trends observed in WL rim pyroxenes. Fig. 11

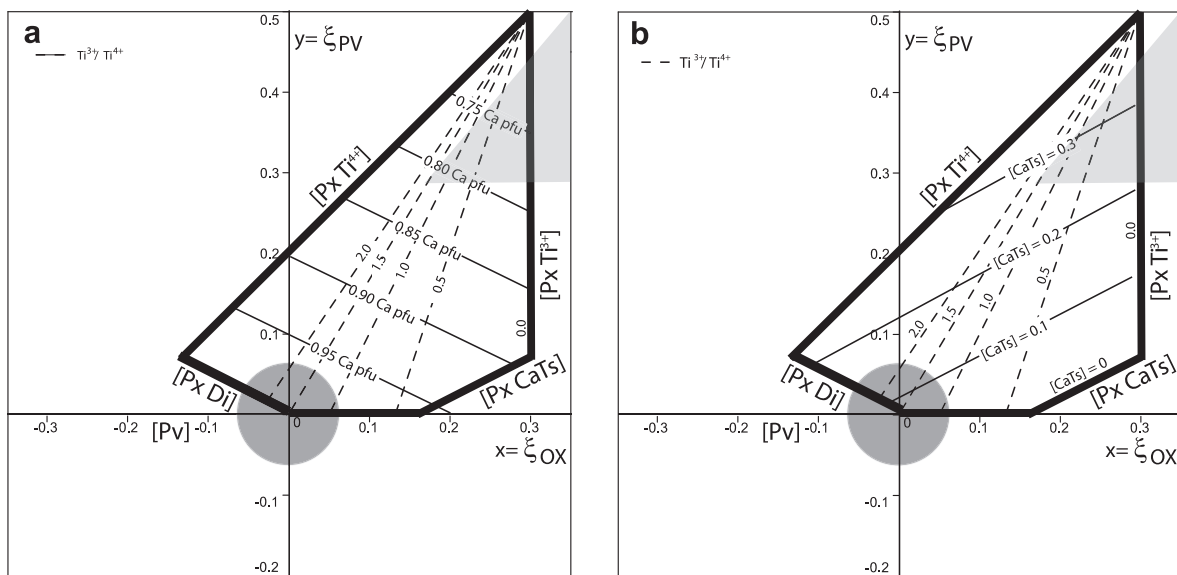
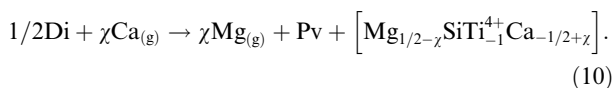


Fig. 11. Reaction space contoured for Ca pfu (a) and [CaTs] in pyroxene (b). The CaTs component is defined in the text. Dashed contours correspond to $\text{Ti}^{3+}/\text{Ti}^{4+}$; bold lines correspond to the boundaries of the reaction space.

shows that oxidation of titanium during pyroxene growth requires a lowering of Ca pfu in the product pyroxene (Fig. 11a). It is also accompanied by an increase in the CaTs component to accommodate the Al that was previously in the Ti^{4+} -pyroxene structure (Fig. 11b). Both of these trends are indeed observed in WL rim pyroxenes (see Table 2).

The predicted [Ca] between 0.70 and 0.80 pfu is lower than the observed WL rim values of [Ca] = 0.83–1.00 pfu, suggesting that reaction (EX) was important during WL rim formation. This reaction was not included in Figs. 10 and 11. We can incorporate the (EX) reaction by combining it with (PV), the ordinate in Figs. 10 and 11, to yield a reaction with an adjustable parameter to account for the observed [Ca]:



Here χ defines the extent of Mg–Ca exchange between pyroxene and the gas phase. When $\chi > 0.5$, WL rim formation occurs in an environment where Ca is condensing and Mg is volatile. The result is that the pyroxene composition, represented by the exchange component in reaction (9), becomes enriched in diopside at the expense of the enstatite. Enstatite is a product of (OX). This reaction alone would produce pyroxene with considerably lower Ca pfu than what we observe in the WL rim. It should be noted that Al-rich diopside in the outer layer of the WL rim of Leoville 144A has [Ca] = 0.96 pfu, supporting its formation. Our WL rim analyses are consistent with $\chi = 0.65$ –0.75.

A few WL rim pyroxenes also apparently contain more diopside than predicted by (OX) and (PV). The direct condensation of diopside from the gas phase most likely accounts for this increase.

4.5. Alteration

Other authors have argued that the absence of Ti^{3+} could be a result of alteration preceding accretion (Simon et al., 2009). This alteration hypothesis is weakened by the recent measurements of titanium valence state in hibonite and Ti-rich pyroxene from Murchison (CM2) inclusions. Simon et al. measured high levels of Ti^{3+} in the structure of these pyroxenes that are consistent with interior CAI values (Simon et al., 2009). Since Murchison has been extensively altered by fluid, and yet retained Ti^{3+} in matrix minerals, we assume Leoville, a considerably less altered rock, will do so as well. Analysis of a Semarkona chondrule also reveals Ti^{3+} -rich pyroxene (Simon et al., 2008). This meteorite also records evidence of aqueous alteration, yet oxidation of titanium is not observed in the pyroxene (Sears et al., 1995). Wark–Lovering rim areas analyzed by EMPA and discussed here do not display evidence for melilite replacement by anorthite, a tell-tale signature of alteration. This replacement feature is not commonly observed in the WL rim of Leoville 144A, though Simon et al. do report an occurrence of this texture (Simon et al., 2007).

5. CONCLUSIONS

We see no definitive difference in estimates for the valence state of Ti obtained by electron microprobe and those obtained by XANES for Leoville 144A CAI. Both data sets indicate more oxidizing conditions than those recorded by CAI interiors. We show here that pollution of our pyroxene analyses by spinel cannot explain the lower pyroxene $\text{Ti}^{3+}/\text{Ti}^{4+}$ in the rims of the CAI. Mixing from other nearby phases is also ruled out. The Al, Ti-rich pyroxenes in the Wark–Lovering rim of Leoville 144A therefore support a more oxidizing environment for WL formation. This is consistent with a mechanism for WL rim growth in response to a change from those imposed by a gas of solar composition to conditions closer to those represented by most meteorite groups.

ACKNOWLEDGEMENTS

We would like to acknowledge support from the NASA Cosmochemistry program (EDY) and the NASA Astrobiology Institute. We thank Dr. Sara Russell of the Natural History Museum of London for access to CAI Leoville 144A. Thank you also to Dr. Larry Grossman and Dr. Steven Simon for access to CAI Ef3.

APPENDIX A. SUPPLEMENTARY DATA

Supplementary data associated with this article can be found, in the online version, at doi:10.1016/j.gca.2010.09.042.

REFERENCES

- Amelin Y., Krot A. N., Hutcheon I. D. and Ulyanov A. A. (2002) Lead isotopic ages of chondrules and calcium–aluminum-rich inclusions. *Science* **297**(5587), 1678–1683.
- Beckett J. R. and Grossman L. (1986) Oxygen fugacities in the solar nebula during crystallization of fassaite in Allende inclusions. *Lunar Planet. Sci. XVII*, 36–37.
- Clayton R. N., Grossman L. and Mayeda T. K. (1973) Component of primitive nuclear composition in carbonaceous meteorites. *Science* **182**, 485–488.
- Dowty E. and Clark J. R. (1973) Crystal structure refinement and optical properties of a Ti^{3+} fassaite from the Allende meteorite. *Amer. Min.* **58**, 230–242.
- Dyl K. A., Simon J. I., Russell S. S. and Young E. D. (2005) Rapidly changing oxygen fugacity in the early solar nebula recorded by CAI rims. *Lunar and Planet. Sci. XXXVI*. #1531 (abstr.).
- Dyl K. A., Young E. D. and Simon J. I. (2008) Reassessing titanium valence state in the Wark–Lovering rim of a Leoville CAI: Further evidence for an oxidizing nebular environment for Wark–Lovering rim formation. *Lunar and Planet. Sci. XXXIX*. #1391 (abstr.).
- Fahey A. J., Zinner E. K., Crozaz G. and Kornacki A. S. (1987) Microdistributions of Mg isotopes and REE abundances in a Type A calcium–aluminum-rich inclusion from Efremovka. *Geochim. et Cosmochim. Acta* **51**(12), 3215–3229.
- Grossman L. (1975) Petrography and mineral chemistry of Ca-rich inclusions in the Allende meteorite. *Geochim. Cosmochim. Acta* **39**, 443–454.

- Krot A. N., Fegley B., Lodders K. and Palme H. (2000) Meteoritical and astrophysical constraints on the oxidation state of the solar nebula. The University of Arizona Press, p. 1019.
- MacPherson G., Grossman J. N., Beckett J. R. and Allen J. M. (1981) Origin of rims on coarse-grained inclusions in the Allende meteorite. *Proc. Lunar Planet. Sci. Conf. 12th*, 1074–1091.
- Murrell M. T. and Burnett D. S. (1987) Actinide chemistry in Allende Ca–Al-rich inclusions. *Geochim. et Cosmochim. Acta* **51**(4), 985–999.
- Ruzicka A. (1997) Mineral layers around coarse-grained, Ca–Al-rich inclusions in CV3 carbonaceous chondrites: Formation by high-temperature metasomatism. *J. Geophys. Res.-Planets* **102**(E6), 13387–13402.
- Sears D. W. G., Morse A. D., Hutchison R., Guimon R. K., Jie Lu., Alexander C. M. O. D., Benoit P. H., Wright I., Pillinger C., Xie Tian. and Lipschutz M. E. (1995) Metamorphism and aqueous alteration in low petrographic type ordinary chondrites. *Meteoritics* **30**, 169–181.
- Simon J. J. I., Young E. D., Russell S. S., Tonui E. K., Dyl K. A. and Manning C. E. (2005) A short timescale for changing oxygen fugacity in the solar nebula revealed by high-resolution ^{26}Al - ^{26}Mg dating of CAI rims. *Earth and Planet. Sci. Lett.* **238**(3–4), 272–283.
- Simon S. S. B., Sutton S. R. and Grossman L. (2007) Valence of titanium and vanadium in pyroxene in refractory inclusion interiors and rims. *Geochim. et Cosmochim. Acta* **71**(12), 3098–3118.
- Simon S. S. B., Sutton S. R. and Grossman L. (2008) Constraints on the oxidation state of chondrule precursors from titanium XANES analysis of Semarkona chondrules. *Lunar and Planet. Sci. XXXIX* **39**, 1352.
- Simon S. S. B., Sutton S. R. and Grossman L. (2009) First Ti-XANES analyses of refractory inclusions from Murchison. *Lunar and Planet. Sci. XL*, #1626 (abstr.).
- Stolper E. Paque J. and Rossman G. R. (1982) The influence of oxygen fugacity and cooling rate on the crystallization of Ca–Al inclusions from Allende. *Lunar and Planet. Sci. XIII*, 772–773.
- Thompson J. B. J. (1982a) Composition space. An algebraic and geometric approach. *Rev. Min.* **10**, 1–32.
- Thompson J. B. J. (1982b) Reaction space. An algebraic and geometric approach. *Rev. Min.* **10**, 33–52.
- Wark D. A. and Lovering J. F. (1977) Marker events in the early evolution of the solar system: Evidence from rims on Ca–Al-rich inclusions in carbonaceous chondrites. *Proc. Lunar Planet. Sci. Conf. 8th*, 95–112.
- Yagi K. and Onuma K. (1967) The joint $\text{CaMgSi}_2\text{O}_6$ - $\text{CaTiAl}_2\text{O}_6$ and its bearings on the titanaugites. *J. Fac. Sci. Hokkaido Univ. Ser. IV* **13**(4), 463–483.

Associate editor: Alexander N. Krot